



Effect of electron-phonon scattering on the anomalous Hall conductivity of Fe₃Sn: A kagome ferromagnetic metal

Achintya Low, Susanta Ghosh, Soumya Ghorai , and Setti Thirupathiah 

Department of Condensed Matter and Materials Physics, S. N. Bose National Centre for Basic Sciences,
JD Block, Salt Lake, Sector III, Kolkata, West Bengal 700106, India



(Received 1 April 2023; accepted 21 August 2023; published 5 September 2023)

We report on magnetic and magnetotransport studies of the kagome ferromagnetic metal Fe₃Sn. Our studies reveal a large anomalous Hall conductivity σ_{zx} in this system, mainly contributed by temperature-independent intrinsic Hall conductivity ($\sigma_{zx}^{\text{int}} = 485 \pm 60 \text{ S cm}^{-1}$) and temperature-dependent extrinsic Hall conductivity σ_{zx}^{ext} due to skew scattering. Although the σ_{zx}^{ext} value is large and almost equivalent to the intrinsic Hall conductivity at low temperatures, it drastically decreases with increasing temperature, following the relation $\sigma_{zx}^{\text{ext}} = \frac{\sigma_{zx0}^{\text{ext}}}{(\sigma T + 1)^2}$, under the influence of electron-phonon scattering. The presence of electron-phonon scattering in this system is also confirmed by the linear dependence of the longitudinal electrical resistivity at higher temperatures [$\rho(T) \propto T$]. We further find that Fe₃Sn is a soft ferromagnet with an easy axis of magnetization lying in the *ab* plane of the crystal with a magnetocrystalline anisotropy energy density as large as $1.02 \times 10^6 \text{ J m}^{-3}$.

DOI: [10.1103/PhysRevB.108.094404](https://doi.org/10.1103/PhysRevB.108.094404)

I. INTRODUCTION

The Hall effect, due to which fast-moving charge carriers get deflected transversely under external magnetic fields in metals and semiconductors [1], has recently been used in many real-life technological applications [2,3]. While an ordinary Hall effect has been noticed in nonmagnetic metals, an anomalous Hall effect (AHE) was found in collinear ferromagnetic metals [4,5] and in noncollinear antiferromagnetic (AFM) metals [6,7]. Moreover, the anomalous Hall effect produces substantially higher Hall resistivity than the ordinary Hall effect, and the field-dependent Hall resistivity scales perfectly with magnetization [4,5]. Although the origin of the AHE in noncollinear AFM metals is widely understood by the presence of the nonzero Berry phase in momentum space, several mechanisms were proposed to understand the AHE in collinear ferromagnets.

Foremost, Karplus and Luttinger (KL) predicted that the AHE in ferromagnetic metals originates from the interband scattering of the charge carriers under spin-orbit coupling [8], which was recently connected to the Berry curvature of the electronic state of solids [9]. Since the KL theory does not take into account the impurity scattering effects and mainly talks about the intrinsic band structure, it is considered as the intrinsic theory of AHE. Later on, Smit *et al.* proposed an extrinsic theory of AHE by incorporating the impurity scattering [10]. The extrinsic AHE happens through two scattering mechanisms, (i) the skew scattering, whereby the charge carriers scatter asymmetrically via the localized magnetic impurities [10], and (ii) the side jump, whereby the charge carrier takes a small side jump upon scattering with impurity under spin-orbit coupling [11,12]. Although

many ferromagnetic metals are known to show the AHE [5], kagome ferromagnets are quite fascinating systems because they show an intrinsic geometrical frustration, leading to several exotic electronic properties, such as flat bands near the Fermi level [13–16], the quantum spin-liquid ground state [17,18], the Chern insulating state [19,20], Weyl fermions [21–23], Dirac fermions [21,24,25], and magnetic topological skyrmions [26,27], manifesting the anomalous and topological Hall effects.

Thus, the ferromagnetic metal Co₃Sn₂S₂ is found to exhibit giant intrinsic anomalous Hall conductivity ($\sigma_{xy} \approx 505 \text{ S cm}^{-1}$) [28] due to the presence of Weyl nodes near the Fermi level [29], and Fe₃Sn₂ is found to show extremely large anomalous Hall conductivity ($\sigma_{xy} \approx 1150 \text{ S cm}^{-1}$) [30] below 2 K and large topological Hall conductivity ($-0.875 \mu\Omega \text{ cm}$) above room temperature [31,32]. On the other hand, recently, a few reports on polycrystalline Fe₃Sn suggested it is a ferromagnetic metal in which the Fe atoms form a kagome network in the *ab* plane. Further, it was also shown that Fe₃Sn exhibits a large magnetocrystalline anisotropy energy [33,34] in addition to the anomalous Nernst effect [35]. Although the previous report showed temperature-dependent anomalous Hall conductivity to some extent, a thorough understanding of the anomalous Hall effect in Fe₃Sn is still missing, especially the influence of electron-phonon scattering on the anomalous Hall conductivity.

Fe₃Sn belongs to the Ni₃Sn-type family of crystal structure with an in-plane kagome network. Unlike its sister compound Mn₃Sn, which is a noncollinear antiferromagnet metal, Fe₃Sn is a collinear in-plane (*ab* plane) ferromagnetic metal. In this paper, we mainly focus on the anomalous Hall effect of Fe₃Sn as a function temperature. For this, we have grown high-quality single crystals of Fe₃Sn and performed magnetic and magnetotransport studies. Our results unravel two important contributions to the total Hall conductivity of Fe₃Sn.

*setti@bose.res.in

One of them is the temperature-independent intrinsic Hall conductivity originating from the electronic band structure, and the other one is the temperature-dependent extrinsic Hall conductivity originating from the asymmetric skew scattering. Most importantly, we observe that the extrinsic skew-scattering Hall conductivity strongly depends on the inelastic electron-phonon scattering rate γ , $\sigma_{zx}^{\text{ext}} = \frac{\sigma_{zx0}^{\text{ext}}}{(\gamma/\gamma_0+1)^2}$. In addition, the linear dependence of the longitudinal electrical resistivity confirms the presence of electron-phonon scattering at higher temperatures. We further show that Fe_3Sn is a soft ferromagnet with an easy axis of magnetization lying parallel to the ab plane. We derive a magnetocrystalline anisotropy energy density as large as $1.02 \times 10^6 \text{ J m}^{-3}$.

II. EXPERIMENTAL DETAILS

High-quality single crystals of Fe_3Sn were grown by the solid-state crystal growth (SSCG) technique. In the SSCG method, the crystals are grown out of polycrystalline matrix. Initially, Fe powder (99.99%, Stern Chemicals) and Sn powder (99.995%, Alfa Aesar) were taken in stoichiometric ratio, ground thoroughly, and heated at 810°C for 7 days. As-prepared Fe_3Sn powder was again ground and pressed into a pellet, which was then annealed at 810°C for another 45 days. Several small rod-shaped shiny crystals with a typical size of $1 \times 0.2 \times 0.2 \text{ mm}^3$ were grown on the surface of the pellet. The x-ray diffraction (XRD) technique was performed on a rod-shaped single crystal and on the crushed crystals using a Rigaku SmartLab 9 kW Cu K_α x-ray source. Elemental analysis was done using energy dispersive x-ray spectroscopy (EDS) and suggests an actual chemical composition of $\text{Fe}_{2.98}\text{Sn}$, which is very close to the nominal composition of Fe_3Sn . For the electrical transport and magnetotransport measurements linear four-probe and Hall probe connections were made, respectively, using copper wire and silver paint. Magnetic and magnetotransport measurements were carried out on a 9 T physical properties measurement system (Quantum Design DynaCool) using the vibrating-sample magnetometer and electrical transport options. To eliminate the longitudinal voltage contribution due to any misalignment of the connections, the Hall resistivity was measured by applying both positive and negative magnetic fields, and average Hall resistivity was calculated by $\rho_H = \frac{\rho_H(H) - \rho_H(-H)}{2}$.

III. RESULTS AND DISCUSSION

Figure 1(a) depicts the schematic crystal structure of Fe_3Sn , where the Fe atoms form a kagome structure with Sn sitting at the center of the kagome lattice. Figure 1(b) shows the powder XRD pattern of crushed Fe_3Sn single crystals, confirming the hexagonal Ni_3Sn -type crystal structure with space group $P6_3/mmc$ (No. 194). The inset in Fig. 1(b) depicts the XRD performed on a rod-shaped single crystal, showing the intensity of reflections from the $(02\bar{2}0)$ Bragg plane, suggesting that the length of rod-shaped crystals is parallel to the c axis. Rietveld refinement performed on the powder XRD of crushed single crystals using the FULLPROF software [36] derived lattice parameters $a = b = 5.4631(4) \text{ \AA}$ and $c = 4.3552(4) \text{ \AA}$, in good agreement with previous reports [33].

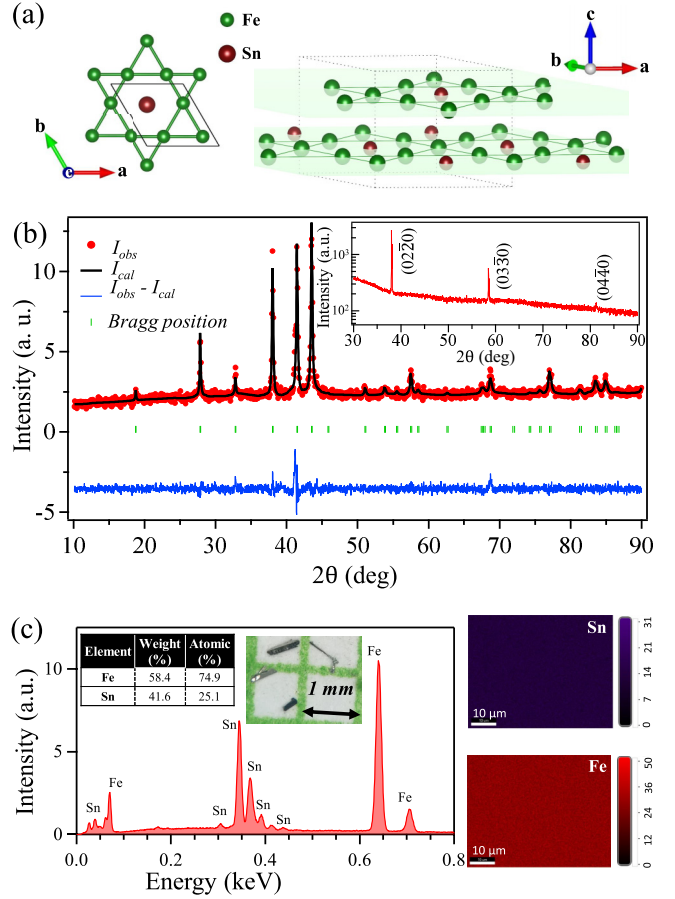


FIG. 1. (a) Schematic crystal structure and kagome lattice of Fe_3Sn . (b) Powder XRD pattern of crushed Fe_3Sn single crystals. The inset in (b) shows intensity reflections correspond to $(02\bar{2}0)$ Bragg planes. The left panel in (c) presents the EDS spectra of Fe_3Sn along with tabulated elemental ratios and a photographic image showing typical Fe_3Sn single crystals. The right panels in (c) show the elemental mapping of measured single crystals for Fe and Sn.

The left panel of Fig. 1(c) shows the EDS data from which the atomic and weight percentages of the elements are tabulated in the top left inset. A photographic image of typical Fe_3Sn single crystals is shown in the right inset in Fig. 1(c). Elemental mapping performed for Fe and Sn using the EDAX is shown in the right panel of Fig. 1(c), implying good homogeneity of single crystals.

Temperature-dependent magnetization $M(T)$ between 2 and 300 K performed on an Fe_3Sn single crystal with the field H applied parallel to the y axis ($H \parallel y$) and parallel to the z axis ($H \parallel z$) in the field-cooled mode is shown in Fig. 2(a). From Fig. 2(a) it is evident that below 300 K, $M(T)$ is completely temperature independent. Figure 2(b) shows $M(T)$ performed between 300 and 800 K on an Fe_3Sn pellet in the zero-field-cooled mode in order to identify the ferromagnetic transition. From Curie-Weiss fitting of the inverse susceptibility $\chi^{-1}(T)$, using the formula $\chi = \frac{C}{T-\theta}$, we derive a Curie constant of $C = 7.1 \pm 0.1 \text{ emu mol}^{-1} \text{ Oe}^{-1} \text{ K}^{-1}$ and a Curie-Weiss temperature of $\theta = 689 \pm 2 \text{ K}$, which are consistent with a previous report [33]. The effective magnetic moment of

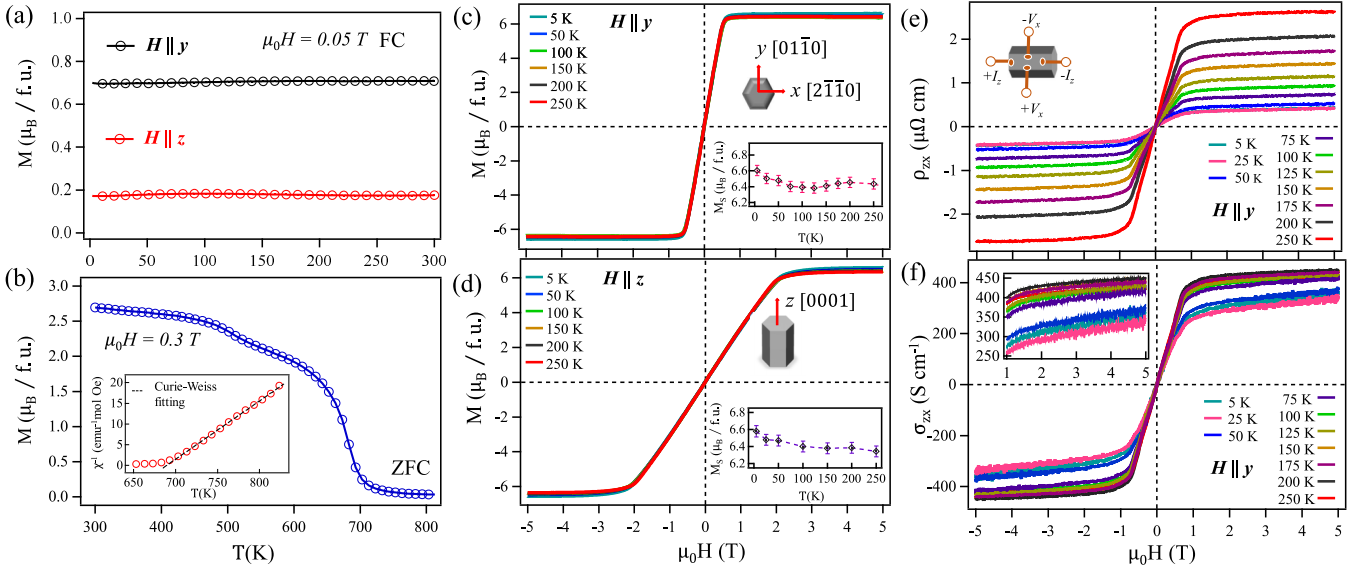


FIG. 2. (a) and (b) Magnetization measured as a function of temperature for Fe_3Sn single crystals and pellets, respectively. The inset in (b) is the Curie-Weiss fitting of the inverse susceptibility plotted as a function of temperature. (c) and (d) The magnetization isotherms $M(H)$ for $H \parallel y$ and $H \parallel z$, respectively. The insets in (c) and (d) show the saturation magnetization. (e) and (f) Hall resistivity and Hall conductivity, respectively, plotted as a function of field at various sample temperatures for $H \parallel y$.

the Fe atom in Fe_3Sn is found to be $\mu_{\text{eff}}(\text{Fe}) = 2.51\mu_B$ using the relation $\mu_{\text{eff}} = 2.828\sqrt{C}$ [37].

Figures 2(c) and 2(d) depict the magnetization isotherms $M(H)$ measured at various sample temperatures for $H \parallel y$ and $H \parallel z$, respectively. The saturation field for $H \parallel y$ is around 0.5 T, whereas it is 2 T for $H \parallel z$, clearly suggesting that Fe_3Sn has an easy axis of magnetization parallel to the ab plane. Also, the absence of hysteresis in the $M(H)$ data for the field applied parallel to both directions makes this system a good soft ferromagnet. The saturation magnetic moment per Fe atom is found to be $M_s = 2.2\mu_B$, which is close to the value of the effective magnetic moment $\mu_{\text{eff}} = 2.51\mu_B$. From the magnetization isotherms shown in Figs. 2(c) and 2(d), we estimate the magnetocrystalline anisotropic energy density $K_u = 1.02 \times 10^6 \text{ J m}^{-3}$ using the relation $K_u = \mu_0 \int_0^{M_s} [H_y(M) - H_z(M)] dM$ after excluding the geometrical demagnetization factor [38]. See the Supplemental Material for more details on the calculations of the demagnetization factor [39]. Here, M_s represents saturation magnetization, and H_z and H_y represent $H \parallel z$ and $H \parallel y$, respectively.

The Hall resistivity ρ_{zx} as a function of field is shown in Fig. 2(e) at various sample temperatures. Here, the current is applied along the z axis, and the magnetic field is applied along the y axis to measure the Hall voltage along the x axis of the crystal, as depicted in the inset in Fig. 2(e). It is evident from Fig. 2(e) that Fe_3Sn shows an anomalous Hall effect with a small normal Hall effect that is visible at very high temperatures. Next, the Hall conductivity σ_{zx} is calculated using the formula $\sigma_{zx} = -\frac{\rho_{zx}}{\rho_{xx}^2 + \rho_{zz}^2}$, where ρ_{zz} is the longitudinal resistivity measured along the z axis of the crystal. Figure 2(f) shows σ_{zx} plotted as a function of field, in which we observe a large anomalous Hall conductivity in the range of 410–425 S cm^{-1} between 75 and 250 K when measured at 5 T, and a sudden drop to 370 S cm^{-1} is

observed upon lowering the sample temperature below 75 K. Although the high-temperature Hall conductivity obtained in this study is consistent with a previous report made on polycrystalline Fe_3Sn [35], the low-temperature Hall conductivity of 200 S cm^{-1} at 2 K observed in Ref. [35] is significantly smaller than our findings ($\approx 370 \text{ S cm}^{-1}$ at 5 K).

Next, Fig. 3(a) depicts the temperature-dependent longitudinal resistivity ρ_{zz} measured with current applied along the z axis of the crystal. We notice that ρ_{zz} quadratically depends on the temperature ($\rho_{zz} \propto T^2$) up to ≈ 75 K, demonstrating a Fermi-liquid-type nature of the resistivity at low temperatures [40]. Nevertheless, above 75 K, ρ_{zz} shows linear dependence on the temperature ($\rho_{zz} \propto T$) due to strong electron-phonon interaction [41]. The temperature-dependent resistivity profile of our Fe_3Sn single crystal is consistent with a previous report on polycrystalline Fe_3Sn [35]. Particularly, the linear dependence of ρ_{zz} above 75 K is in very good agreement with Ref. [35]. The temperature-dependent longitudinal conductivity σ_{zz} is also shown in Fig. 3(a). In general, the total Hall resistivity presented in Fig. 2(e) can be expressed by the empirical formula $\rho_H = \rho_H^N + \rho_H^A$ [5]. Here, the first term represents the normal Hall contribution $\rho_H^N = \mu_0 R_0 H$, and the second term represents the anomalous Hall contribution, which in turn depends on the magnetization M as $\rho_H^A = \mu_0 R_S M$. Here, R_0 and R_S are the normal and anomalous Hall coefficients, respectively. Further, with the help of the normal Hall coefficient R_0 one can calculate the charge carrier q density using the relation $n = \frac{1}{R_0 |q|}$. Since the field-dependent anomalous Hall effect is a replica of magnetization, anomalous Hall resistivity saturates beyond a critical field and becomes almost field independent, while the normal Hall resistivity linearly depends on field.

Thus, in order to separate the anomalous Hall resistivity from the normal Hall contribution, we fitted the high-field

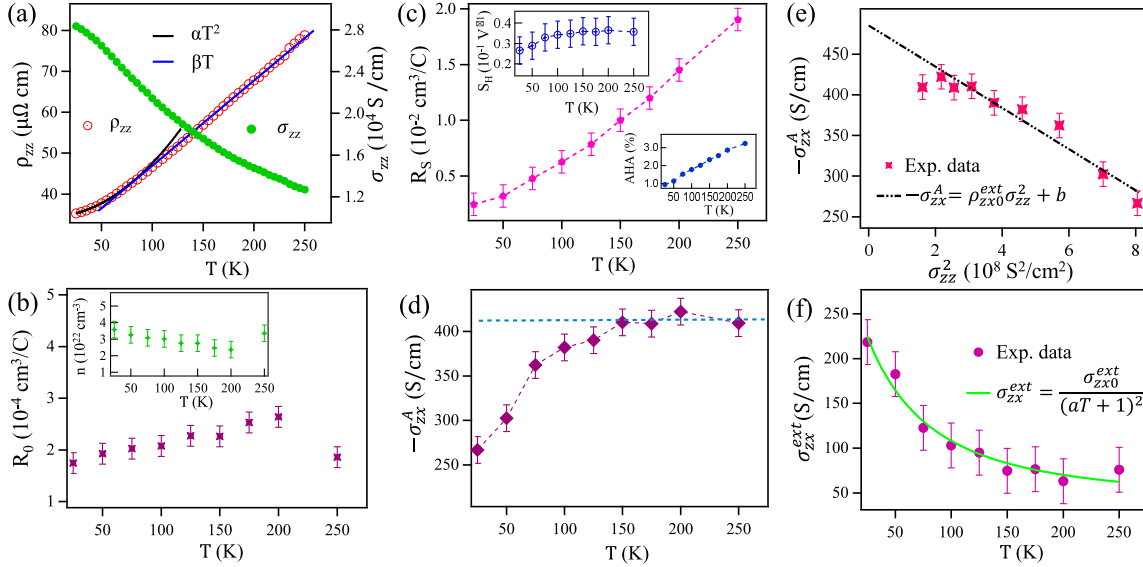


FIG. 3. (a) Longitudinal electrical resistivity ρ_{zz} and electrical conductivity σ_{zz} plotted as a function of temperature. (b) and (c) Normal Hall coefficient R_0 and anomalous Hall coefficient R_S plotted as a function of temperature, respectively. The charge carrier density n is shown in the inset in (b). Top inset in (c) shows the anomalous Hall scale factor S_H , and the bottom inset in (c) shows the anomalous Hall angle percentage [AHA(%)]. (d) Anomalous Hall conductivity $-\sigma_{zx}^A$ as a function of temperature. (e) $-\sigma_{zx}^A$ vs σ_{zz}^2 plot. The dashed line in (e) is a linear fitting using the relation $-\sigma_{zx}^A = \rho_{zx0}^{\text{ext}} \sigma_{zz}^2 + b$. (f) Extrinsic anomalous Hall conductivity σ_{zx}^{ext} plotted as a function of temperature. The solid green curve in (f) is a fit for the equation $\sigma_{zx}^{\text{ext}} = \frac{\sigma_{zx0}^{\text{ext}}}{(aT+1)^2}$.

region of the total Hall resistivity with a linear function of field and subtracted the normal Hall contribution from the total Hall resistivity. In this way, we extracted various important parameters such as the normal (R_0) and anomalous (R_S) Hall coefficients. Figure 3(b) depicts R_0 plotted as a function of temperature. The positive R_0 values throughout the measured temperature range as observed in Fig. 3(b) suggest hole-carrier-dominant electrical transport in Fe_3Sn . The inset in Fig. 3(b) demonstrates almost temperature-independent hole carrier density n_h which is of the order of $\sim 10^{22} \text{ cm}^{-3}$, suggesting Fe_3Sn is a good metal. Figure 3(c) shows the anomalous Hall coefficient R_S plotted as a function of temperature. The top inset in Fig. 3(c) presents the anomalous Hall scaling factor $S_H = \frac{-\sigma_{zx}^A}{M} = \frac{\mu_0 R_S}{\rho_{zz}^2} (\cong \frac{\rho_{zx}^A}{M \rho_{zz}^2})$, plotted as a function of temperature. We observe that S_H is almost temperature independent within the error bars. Moreover, the value of $S_H = 0.03 \pm 0.01 \text{ V}^{-1}$ derived in this study is within the range of $0.01\text{--}0.2 \text{ V}^{-1}$ for any typical ferromagnetic metal [42,43]. The bottom inset in Fig. 3(c) shows the temperature-dependent anomalous Hall angle (AHA), defined as the deviation of electron flow from the current direction, which is calculated using the formula $\text{AHA} = \frac{\sigma_{zx}^A}{\sigma_{zz}} \times 100(\%)$. We clearly notice that $\text{AHA} \approx 3\%$ at 250 K and decreases with temperature. The value of $\text{AHA} \approx 3\%$ is close to the AHA values reported for the similar kagome ferromagnetic system Fe_3Sn_2 ($\approx 1.1\%$) [43] and kagome antiferromagnetic systems such as Mn_3Sn ($\approx 3.2\%$) [6] and Mn_3Ge ($\approx 5\%$) [7] but much smaller than the value for the shandite kagome ferromagnet $\text{Co}_3\text{Sn}_2\text{S}_2$ ($\approx 20\%$) [28].

Several mechanisms were proposed to understand the anomalous Hall effect in magnetic and nonmagnetic metals.

In most of the proposals, the anomalous Hall resistivity ρ_{zx}^A is represented mainly by the function of longitudinal resistivity ρ_{zz} , $\rho_{zx}^A = f(\rho_{zz})$. (i) More explicitly, the intrinsic Karplus-Luttinger mechanism of the AHE describes the Hall resistivity $\propto \rho_{zz}^2$ due to the interband scattering in presence of strong spin-orbit coupling [8]. (ii) The extrinsic side-jump mechanism of the AHE describes the Hall resistivity $\propto \rho_{zz}^2$ due to side-jump scattering of charge carriers at the impurities [11]. (iii) The extrinsic skew-scattering mechanism of the AHE describes the Hall resistivity $\propto \rho_{zz}$ due to skew scattering of the charge carrier at the impurities [10], and (iv) a ρ_{zz}^α ($1 < \alpha < 2$) dependence of ρ_{zx}^A was proposed in the case of bad metals [44]. For our case, mechanism (iv) can be ignored because the longitudinal conductivity of Fe_3Sn is found to be $\sigma_{zz} = 31.4 \frac{e^2}{hc}$ (where c is the lattice constant), which is in the metallic regime [45]. Recently, a new mechanism was proposed by Tian, Ye, and Jin (TYJ) [46] in order to understand the AHE in ferromagnetic metals. According to TYJ theory, the anomalous Hall resistivity is described by $\rho_{zx}^A = f(\rho_{zx0}, \rho_{zz})$, which includes the residual resistivity ρ_{zx0} . Thus, following the TYJ theory [46,47], the anomalous Hall resistivity takes the form $\rho_{zx}^A = (\alpha \rho_{zx0} + \beta \rho_{zz}^2) + b \rho_{zz}^2$, and the anomalous Hall conductivity is represented by $-\sigma_{zx}^A = (\alpha \sigma_{zx0}^{-1} + \beta \sigma_{zx0}^{-2}) \sigma_{zz}^2 + b = \rho_{zx0}^{\text{ext}} \sigma_{zz}^2 + b$. Here, α and β are real constants, $\sigma_{zx0} = 1/\rho_{zx0}$ is the residual conductivity, and b is the intrinsic Hall conductivity originating from the momentum space Berry curvature. It is well known that the intrinsic Hall conductivity b is usually temperature independent [5,28] except for systems showing electronic or magnetic phase transitions [9,48]. Since Fe_3Sn shows neither an electronic nor magnetic transition within the measured temperature range of 2–250 K, change in the

Berry phase is not expected. From Fig. 3(d), we notice that the anomalous Hall conductivity is almost constant at higher temperatures but decreases below 150 K. To understand this phenomenon, we employed the TYJ mechanism to fit the data of $-\sigma_{zx}^A$ vs σ_{zz}^2 , as shown in Fig. 3(e), demonstrating a good fit within the error bars. From the fitting, we extracted intrinsic Hall conductivity $b = 485 \pm 60 \text{ S cm}^{-1}$, which is close to the previously reported values for polycrystalline Fe_3Sn ($\approx 500 \text{ S cm}^{-1}$) [35] and predicted by a theoretical calculation ($\approx 600 \text{ S cm}^{-1}$ at E_F) [49].

Next, Fig. 3(f) shows the extrinsic Hall conductivity σ_{zx}^{ext} extracted from the total conductivity by subtracting the intrinsic Hall contribution b . From Fig. 3(f), it is evident that the extrinsic Hall conductivity decreases with increasing sample temperature. Further, the sign of extrinsic Hall conductivity is opposite the intrinsic Hall conductivity, resulting in the reduced total Hall conductivity at lower temperatures. As we know, in the clean limit, for $\hbar/\tau \rightarrow 0$ (τ is the relaxation time) the extrinsic skew-scattering contribution diverges [50]. On the other hand, from Fig. 3(f), we can see that as the sample temperature decreases, the extrinsic Hall conductivity rapidly increases. This observation indicates that skew scattering plays a major role in generating the anomalous Hall conductivity in Fe_3Sn . The longitudinal resistivity ρ_{zz} suggests electron-phonon scattering at higher temperatures in this system. In order to understand the phonon influence on the anomalous Hall conductivity, we employed the mechanism proposed by Shitade and Nagaosa [45], which involves the electron-phonon inelastic scattering rates γ . In this mechanism, the extrinsic Hall conductivity decays with γ following the relation $\sigma_{zx}^{\text{ext}} = \frac{\sigma_{zx0}^{\text{ext}}}{(\gamma/\gamma_0+1)^2}$. Since the inelastic scattering rate is proportional to the longitudinal resistivity [$\gamma \sim (\rho_{zz} - \rho_{zz0})$] and $\rho_{zz} - \rho_{zz0}$ linearly depends on temperature [$(\rho_{zz} - \rho_{zz0}) \propto T$] above 75 K [see Fig. 3(a)], we can rewrite the equation as $\sigma_{zx}^{\text{ext}} = \frac{\sigma_{zx0}^{\text{ext}}}{(aT+1)^2}$. Here, $a = 0.011 \pm 0.003 \text{ K}^{-1}$ represents the measure of the inelastic electron-phonon scattering strength. In this way, we can fit the σ_{zx}^{ext} data very well, as shown in Fig. 3(f). Thus, our results clearly demonstrate the influence of electron-phonon interaction on the

extrinsic skew-scattering anomalous Hall conductivity, which decreases with increasing temperature. Finally, we would like to mention here that recently, a paper on the magnetic study of Fe_3Sn single crystals appeared [51]. The magnetic properties presented in that study are consistent with our findings. Particularly, the magnetocrystalline anisotropy energy density of $1.23 \times 10^6 \text{ J m}^{-3}$ reported in Ref. [51] is in good agreement with the value of $1.02 \times 10^6 \text{ J m}^{-3}$ found in this study.

IV. SUMMARY

In summary, we successfully grew high-quality single crystals of Fe_3Sn . In this study, we mainly focused on understanding the anomalous Hall effect as a function temperature. Our results unravel two main contributions to the total Hall conductivity of Fe_3Sn . One of them is the temperature-independent intrinsic Hall conductivity originating from the electronic band structure, and the other one is the temperature-dependent extrinsic Hall conductivity due to the asymmetric skew scattering. Most importantly, we found that the extrinsic skew-scattering Hall conductivity is significantly influenced by the electron-phonon scattering at higher temperatures and obeys the relation $\sigma_{zx}^{\text{ext}} = \frac{\sigma_{zx0}^{\text{ext}}}{(aT+1)^2}$. In addition, the longitudinal electrical resistivity ρ_{zz} confirms the presence of electron-phonon scattering as the resistivity linearly depends on the temperature. We showed that Fe_3Sn is a soft ferromagnet with easy-axis magnetization lying parallel to the ab plane. We estimated a magnetocrystalline anisotropic energy density as large as $1.02 \times 10^6 \text{ J m}^{-3}$ in Fe_3Sn .

ACKNOWLEDGMENTS

The authors thank the Science and Engineering Research Board (SERB), Department of Science and Technology (DST), India, for the financial support (Grant No. SRG/2020/000393). This research has made use of the Technical Research Centre (TRC) Instrument Facilities of the S. N. Bose National Centre for Basic Sciences, established under the TRC project of the Department of Science and Technology, Government of India.

-
- [1] E. H. Hall, On a new action of the magnet on electric currents, *Am. J. Math.* **2**, 287 (1879).
- [2] R. S. Popovic, *Hall Effect Devices* (CRC Press, Boca Raton, FL, 2003).
- [3] E. Ramsden, *Hall-Effect Sensors: Theory and Application* (Elsevier, Oxford, UK, 2011).
- [4] E. Hall, On the new action of magnetism on a permanent electric current, *London, Edinburgh, Dublin Philos. Mag. J. Sci.* **10**, 301 (1880).
- [5] N. Nagaosa, J. Sinova, S. Onoda, A. H. MacDonald, and N. P. Ong, Anomalous Hall effect, *Rev. Mod. Phys.* **82**, 1539 (2010).
- [6] S. Nakatsuji, N. Kiyohara, and T. Higo, Large anomalous Hall effect in a non-collinear antiferromagnet at room temperature, *Nature (London)* **527**, 212 (2015).
- [7] A. K. Nayak, J. E. Fischer, Y. Sun, B. Yan, J. Karel, A. C. Komarek, C. Shekhar, N. Kumar, W. Schnelle, J. Kübler, C. Felser, and S. S. P. Parkin, Large anomalous Hall effect driven by a nonvanishing Berry curvature in the noncollinear antiferromagnet Mn_3Ge , *Sci. Adv.* **2**, e1501870 (2016).
- [8] R. Karplus and J. M. Luttinger, Hall Effect in Ferromagnetics, *Phys. Rev.* **95**, 1154 (1954).
- [9] K. Manna, L. Muechler, T.-H. Kao, R. Stinshoff, Y. Zhang, J. Gooth, N. Kumar, G. Kreiner, K. Koepf, R. Car, J. Kübler, G. H. Fecher, C. Shekhar, Y. Sun, and C. Felser, From Colossal to Zero: Controlling the Anomalous Hall Effect in Magnetic Heusler Compounds via Berry Curvature Design, *Phys. Rev. X* **8**, 041045 (2018).
- [10] J. Smit, The spontaneous Hall effect in ferromagnetics II, *Physica (Amsterdam)* **24**, 39 (1958).
- [11] L. Berger, Side-jump mechanism for the Hall effect of ferromagnets, *Phys. Rev. B* **2**, 4559 (1970).
- [12] S. K. Lyo and T. Holstein, Side-Jump Mechanism for Ferromagnetic Hall Effect, *Phys. Rev. Lett.* **29**, 423 (1972).

- [13] B. Sutherland, Localization of electronic wave functions due to local topology, *Phys. Rev. B* **34**, 5208 (1986).
- [14] E. H. Lieb, Two theorems on the Hubbard model, *Phys. Rev. Lett.* **62**, 1201 (1989).
- [15] D. Leykam, A. Andreanov, and S. Flach, Artificial flat band systems: From lattice models to experiments, *Adv. Phys.: X* **3**, 1473052 (2018).
- [16] C. Wu, D. Bergman, L. Balents, and S. Das Sarma, Flat Bands and Wigner Crystallization in the Honeycomb Optical Lattice, *Phys. Rev. Lett.* **99**, 070401 (2007).
- [17] L. Savary and L. Balents, Quantum spin liquids: A review, *Rep. Prog. Phys.* **80**, 016502 (2017).
- [18] C. Broholm, R. J. Cava, S. A. Kivelson, D. G. Nocera, M. R. Norman, and T. Senthil, Quantum spin liquids, *Science* **367**, eaay0668 (2020).
- [19] C. L. Kane and E. J. Mele, Quantum Spin Hall Effect in Graphene, *Phys. Rev. Lett.* **95**, 226801 (2005).
- [20] H. Huang, Z. Liu, H. Zhang, W. Duan, and D. Vanderbilt, Emergence of a Chern-insulating state from a semi-Dirac dispersion, *Phys. Rev. B* **92**, 161115(R) (2015).
- [21] P. B. Pal, Dirac, Majorana, and Weyl fermions, *Am. J. Phys.* **79**, 485 (2011).
- [22] G. Xu, H. Weng, Z. Wang, X. Dai, and Z. Fang, Chern Semimetal and the Quantized Anomalous Hall Effect in HgCr_2Se_4 , *Phys. Rev. Lett.* **107**, 186806 (2011).
- [23] K. Landsteiner, Anomalous transport of Weyl fermions in Weyl semimetals, *Phys. Rev. B* **89**, 075124 (2014).
- [24] K. S. Novoselov, A. K. Geim, S. V. Morozov, D. Jiang, M. I. Katsnelson, I. V. Grigorieva, S. Dubonos, and A. Firsov, Two-dimensional gas of massless Dirac fermions in graphene, *Nature (London)* **438**, 197 (2005).
- [25] K. Nomura and A. H. MacDonald, Quantum Transport of Massless Dirac Fermions, *Phys. Rev. Lett.* **98**, 076602 (2007).
- [26] N. Nagaosa and Y. Tokura, Topological properties and dynamics of magnetic skyrmions, *Nat. Nanotechnol.* **8**, 899 (2013).
- [27] A. Fert, N. Reyren, and V. Cros, Magnetic skyrmions: Advances in physics and potential applications, *Nat. Rev. Mater.* **2**, 17031 (2017).
- [28] E. Liu, Y. Sun, N. Kumar, L. Muechler, A. Sun, L. Jiao, S.-Y. Yang, D. Liu, A. Liang, Q. Xu, J. Kroder, V. Süß, H. Borrmann, C. Shekhar, Z. Wang, C. Xi, W. Wang, W. Schnelle, S. Wirth, Y. Chen, S. T. B. Goennenwein, and C. Felser, Giant anomalous Hall effect in a ferromagnetic kagome-lattice semimetal, *Nat. Phys.* **14**, 1125 (2018).
- [29] N. Morali, R. Batabyal, P. K. Nag, E. Liu, Q. Xu, Y. Sun, B. Yan, C. Felser, N. Avraham, and H. Beidenkopf, Fermi-arc diversity on surface terminations of the magnetic Weyl semimetal $\text{Co}_3\text{Sn}_2\text{S}_2$, *Science* **365**, 1286 (2019).
- [30] L. Ye, M. Kang, J. Liu, F. von Cube, C. R. Wicker, T. Suzuki, C. Jozwiak, A. Bostwick, E. Rotenberg, D. C. Bell, L. Fu, R. Comin, and J. G. Checkelsky, Massive Dirac fermions in a ferromagnetic kagome metal, *Nature (London)* **555**, 638 (2018).
- [31] Z. Hou, W. Ren, B. Ding, G. Xu, Y. Wang, B. Yang, Q. Zhang, Y. Zhang, E. Liu, F. Xu, W. Wang, G. Wu, X. Zhang, B. Shen, and Z. Zhang, Observation of various and spontaneous magnetic skyrmionic bubbles at room temperature in a frustrated kagome magnet with uniaxial magnetic anisotropy, *Adv. Mater.* **29**, 1701144 (2017).
- [32] H. Li, B. Ding, J. Chen, Z. Li, Z. Hou, E. Liu, H. Zhang, X. Xi, G. Wu, and W. Wang, Large topological Hall effect in a geometrically frustrated kagome magnet Fe_3Sn_2 , *Appl. Phys. Lett.* **114**, 192408 (2019).
- [33] B. C. Sales, B. Sagarov, M. A. McGuire, D. J. Singh, and D. S. Parker, Ferromagnetism of Fe_3Sn and alloys, *Sci. Rep.* **4**, 7024 (2014).
- [34] O. Y. Vekilova, B. Fayyazi, K. P. Skokov, O. Gutfleisch, C. Echevarria-Bonet, J. M. Barandiarán, A. Kovacs, J. Fischbacher, T. Schrefl, O. Eriksson, and H. C. Herper, Tuning the magnetocrystalline anisotropy of Fe_3Sn by alloying, *Phys. Rev. B* **99**, 024421 (2019).
- [35] T. Chen, S. Minami, A. Sakai, Y. Wang, Z. Feng, T. Nomoto, M. Hirayama, R. Ishii, T. Koretsune, R. Arita, and S. Nakatsuji, Large anomalous Nernst effect and nodal plane in an iron-based kagome ferromagnet, *Sci. Adv.* **8**, eabk1480 (2022).
- [36] J. Rodríguez-Carvajal, Recent advances in magnetic structure determination by neutron powder diffraction, *Phys. B: Condens. Matt.* **192**, 55 (1993).
- [37] S. Mugiraneza and A. M. Hallas, Tutorial: A beginner's guide to interpreting magnetic susceptibility data with the Curie-Weiss law, *Commun. Phys.* **5**, 95 (2022).
- [38] R. Prozorov and V. G. Kogan, Effective Demagnetizing Factors of Diamagnetic Samples of Various Shapes, *Phys. Rev. Appl.* **10**, 014030 (2018).
- [39] See Supplemental Material at <http://link.aps.org/supplemental/10.1103/PhysRevB.108.094404> for the calculations of the geometrical demagnetization factor.
- [40] K. Behnia, On the origin and the amplitude of T-square resistivity in Fermi liquids, *Ann. Phys. (Berlin, Ger.)* **534**, 2100588 (2022).
- [41] G. Varelogiannis and E. N. Economou, Small-q electron-phonon scattering and linear dc resistivity in high- T_c oxides, *Europhys. Lett.* **42**, 313 (1998).
- [42] C. Zeng, Y. Yao, Q. Niu, and H. H. Weitering, Linear Magnetization Dependence of the Intrinsic Anomalous Hall Effect, *Phys. Rev. Lett.* **96**, 037204 (2006).
- [43] Q. Wang, S. Sun, X. Zhang, F. Pang, and H. Lei, Anomalous Hall effect in a ferromagnetic Fe_3Sn_2 single crystal with a geometrically frustrated Fe bilayer kagome lattice, *Phys. Rev. B* **94**, 075135 (2016).
- [44] J. M. Lavine, Extraordinary Hall-Effect Measurements on Ni, Some Ni Alloys, and Ferrites, *Phys. Rev.* **123**, 1273 (1961).
- [45] A. Shitade and N. Nagaosa, Anomalous Hall Effect in Ferromagnetic Metals: Role of Phonons at Finite Temperature, *J. Phys. Soc. Jpn.* **81**, 083704 (2012).
- [46] Y. Tian, L. Ye, and X. Jin, Proper Scaling of the Anomalous Hall Effect, *Phys. Rev. Lett.* **103**, 087206 (2009).
- [47] D. Hou, G. Su, Y. Tian, X. Jin, S. A. Yang, and Q. Niu, Multi-variable Scaling for the Anomalous Hall Effect, *Phys. Rev. Lett.* **114**, 217203 (2015).
- [48] N. H. Sung, F. Ronning, J. D. Thompson, and E. D. Bauer, Magnetic phase dependence of the anomalous Hall effect in Mn_3Sn single crystals, *Appl. Phys. Lett.* **112**, 132406 (2018).
- [49] C. Shen, I. Samathrakris, K. Hu, H. K. Singh, N. Fortunato, H. Liu, O. Gutfleisch, and H. Zhang, Thermodynamical and

- topological properties of metastable Fe₃Sn, [npj Comput. Mater.](#) **8**, 248 (2022).
- [50] S. Onoda, N. Sugimoto, and N. Nagaosa, Intrinsic Versus Extrinsic Anomalous Hall Effect in Ferromagnets, [Phys. Rev. Lett.](#) **97**, 126602 (2006).
- [51] L. Prodan, D. M. Evans, S. M. Griffin, A. Östlin, M. Althaler, E. Lysne, I. G. Filippova, S. Shova, L. Chioncel, V. Tsurkan, and I. Kézsmárki, Large ordered moment with strong easy-plane anisotropy and vortex-domain pattern in the kagome ferromagnet Fe₃Sn, [Appl. Phys. Lett.](#) **123**, 021901 (2023).